A multi-physics and multi-scale approach to characterize the viscous layer growth formed on SLM 316L stainless steel during electropolishing in an acid mixture

Aurélien Boucher[a+b], Magali Barthes[c], Luc Froehly[c], Marie-Laure Doche[b], Christine Régent[b], Jean-Yves Hihn[b,1] ,

[a] *SAFRAN TECH, établissement SAFRAN PARIS-SACLAY, F-78 772 Magny-Les-Hameaux*

[b] *Université Marie et Louis Pasteur, CNRS, Institut UTINAM (UMR 6213), équipe SRS, F-25000 Besançon, France*

[c] *Université Marie et Louis Pasteur, CNRS, institut FEMTO-ST, F-25000 Besançon, France*

Abstract

This study aims to provide experimental evidence of the formation and the growth of a viscous layer during the electropolishing of additively manufactured 316L stainless steel parts, using a combination of optical characterization techniques. A tertiary current distribution model was subsequently developed to simulate the electropolishing process and predict the evolution of the viscous layer. The results demonstrate that the viscous layer forms and grows within a specific potential window before being disrupted by gas evolution due to solvent oxidation. Schlieren imaging estimates the thickness of the layer to be approximately 1.4 mm after 5 minutes of polarization at the onset of the polishing plateau—about 1 mm thicker than its natural state without polarization. Particle Image Velocimetry (PIV) confirms the presence of a flow-deprived zone near the surface, roughly 1 mm thick, contrasting with the bulk region where natural convection dominates. A simplified reaction mechanism is proposed, based on experimentally determined electron-transfer kinetics. Metal cations are assumed to be instantly complexed, with the diffusion of the resulting complexes considered equivalent to that of the free complexing agents (phosphates), based on literature values. Using these assumptions, the tertiary current distribution model successfully replicates the growth of the viscous layer. The model's predictions were validated by experimental measurements of metal cation concentrations, supporting the hypothesis that the diffusion of "acceptor" species is the primary driving force behind electropolishing. This work also confirms that phosphate-complexed metal cations diffuse analogously to anions.

1 Introduction

Use of a finishing step to improve overall surface condition is frequently requiered, particularly in the case of Additive Manufacturing (AM). AM lends itself particularly well to the production of mockups to evaluate appearance renders and/or technological properties [1] but with major drawback linked to surface quality, which is often very poor, characterized by the presence of partially melted particles and extremely high roughness (ra $\approx 30\mu m$) [2,3].

Most finishing processes are subtractive, based on removal of a thin layer of material to level the surface. Various types of polishing are available: mechanical, chemical or electrochemical, for example. In comparison, chemical and electrochemical polishing are non-contact processes, which avoid some of the drawbacks of mechanical polishing (tool marks, surface hardening, surface contamination, etc.) As these are based on immersion of the part in a liquid, they offer an easier way to polish complex shapes and internal structures, regardless of metal hardness. The main advantage of electropolishing over chemical polishing lies in the less hazardous nature of baths used, thanks to the contribution of an energy source: the external current. This also helps to achieve a smoother and shinier appearance [4,5].

---

[1] : Corresponding author: Pr. Jean-Yves Hihn
E-mail address: jean-yves.hihn@univ-fcomte.fr

There is as yet no consensus on the mechanisms of electrolytic polishing. In Jacquet's theory [6,7], it is a difference in thickness of the viscous layer, at peak and valley level, that explains the higher dissolution speed of the peaks. According to his theory, the difference in thickness results in an electrical resistance gradient, therefore influencing dissolution rates. In the 1940s, Elmore [8,9] added a diffusion phenomenon to Jacquet's theory. For these authors, the difference in thickness is not sufficient to explain the difference in dissolution rates. There may also be a concentration gradient of metal cations, which do not diffuse quickly enough to the bulk of the electrolyte. This concentration gradient at the electrode surface is proportional to the anodic dissolution current. As a result, when electropolishing is in progress, dissolved metal cations diffuse more rapidly to the core from peaks than from troughs, as there is less distance to travel. These theories are reinforced, supported and substantiated by Landolt [10] and Levich [11], who conclude that electrochemical polishing is achieved through diffusion-controlled dissolution. Other theories, such as that of Hoar et al [12], are based on the formation of an oxide layer on the surface, whose thickness remains constant. Diard et al [13] further developed the diffusion-controlled process theory, describing the role of so-called "acceptor" species that are consumed at the anode. Matlozs et al [14,15] validated this theory using impedance analysis, which confirmed a model mechanism based on limitation of dissolution by the diffusion of "acceptor" species.

Some works [16,17] have already illustrated the ability of an acidic mixture to electropolish AM 316L stainless steel. This is of primary interest because 316L stainless steel is an austenitic steel widely used for its corrosion resistance and excellent mechanical properties. 316L is said to be "stainless" because its surface is protected by a thin passivating layer (of the order of a few nanometers), mainly composed of trivalent chromium oxides (Cr_2O_3). Although this layer provides an effective barrier against generalized corrosion, it can be locally attacked by chloride ions, resulting in pitting corrosion. Nonetheless, it remains one of the most corrosion-resistant everyday materials, which explains why it is so widely used in applications ranging from medical to food, transport (automotive, aeronautical, etc.) and luxury (jewelry and watchmaking in particular) [18]. Its electropolishing enables roughness reduction, as well as increased brightness on as-built additive manufacturing parts. Despite evidence of the electrolyte's ability to electropolish this material, no-one has yet provided a complete study on viscous layer establishment and characterization. However, more recent work than that on the mechanisms has revealed the viscous layer on copper [19] and tungsten [20] for example. Scaling up to larger, more complex parts requires development of simulation tools to assist in preparation of the finishing process and predict optimal operating parameters. Furthermore, simulation is an important asset in understanding mechanisms, as it allows different scenarios to be tested, the results of which can be compared with experimental calibration tests. Despite the emergence of work on simulation of electrolytic coating processes [21], as well as electrochemical machining [22–25], there are very few publications on development of simulation models for the electropolishing process [26,27]. Since the presence of this viscous layer greatly influences this process, it is necessary to characterize the conditions under which it grows and how it remains stable. In addition, simulation models need to be developed that can accurately replicate the behavior of the viscous layer.

The aim of this work is primarily to provide evidence of the presence of the viscous layer during electropolishing of AM 316L SS parts by means of various optical characterizations. Subsequently, a tertiary current distribution model was developed to reproduce the electropolishing process and predict the evolution of the viscous layer.

2   Experimental aspects

2.1   Electropolishing of additive manufacturing parts

Austenitic stainless steel (type 316L) from Laser Additive Manufactured was provided by Volum-e (Blangy-sur-Bresle, France). The specimens are square bars (10mm x 10mm x 100mm). The samples are used as-built without any preparation. The electrolyte consists of an acidic mixture: 45 %$_w$ of commercial 85 %$_w$ of phosphoric acid, 35 %$_w$ of commercial 98 %$_w$ of sulfuric acid, and the last 20 %$_w$ of distilled water.

A pilot cell (Figure 1) was designed with the main constraint of being optically transparent and presenting flat surfaces. For these reasons, poly(methyl methacrylate) (PMMA) sheets with different thicknesses were

used: a 10 mm thick plate to build up the electrolyte tank, and two 1 mm sheets as side walls through which the observations were performed. The cell walls were glued to the SLM stainless steel bar that closes the cell at the bottom. As PMMA is not resistant to highly concentrated mineral acid, each cell was designed as a single-use cell. Temperature monitoring was performed with a thermocouple immersed in the cell. The initial temperature was close to ambient, varying from 20 to 22 °C.

Electropolishing was carried out without agitation, thanks to a classical three-electrode assembly. In this setup, the SS 316L bar acts as the working electrode (anode), while a platinum-plated titanium mesh facing the anode serves as counter-electrode. According to the large amount of sulfuric acid, a mercurous sulfate electrode (MSE) was chosen as a reference electrode. Due to the large active surface area of the SLM parts (S > 10 cm^2), it was not possible to use a laboratory potentiostat, which is limited in current. Hence, a power supply (40 A-30 V), developed specifically for our needs (Micronics Systems™), was used to drive the process either in direct, pulse or dynamic mode. It also enabled potentiostatic control versus a reference electrode in the range ± 20 V/Ref so as to work at constant potential or to plot polarization curves (I=f(E)).
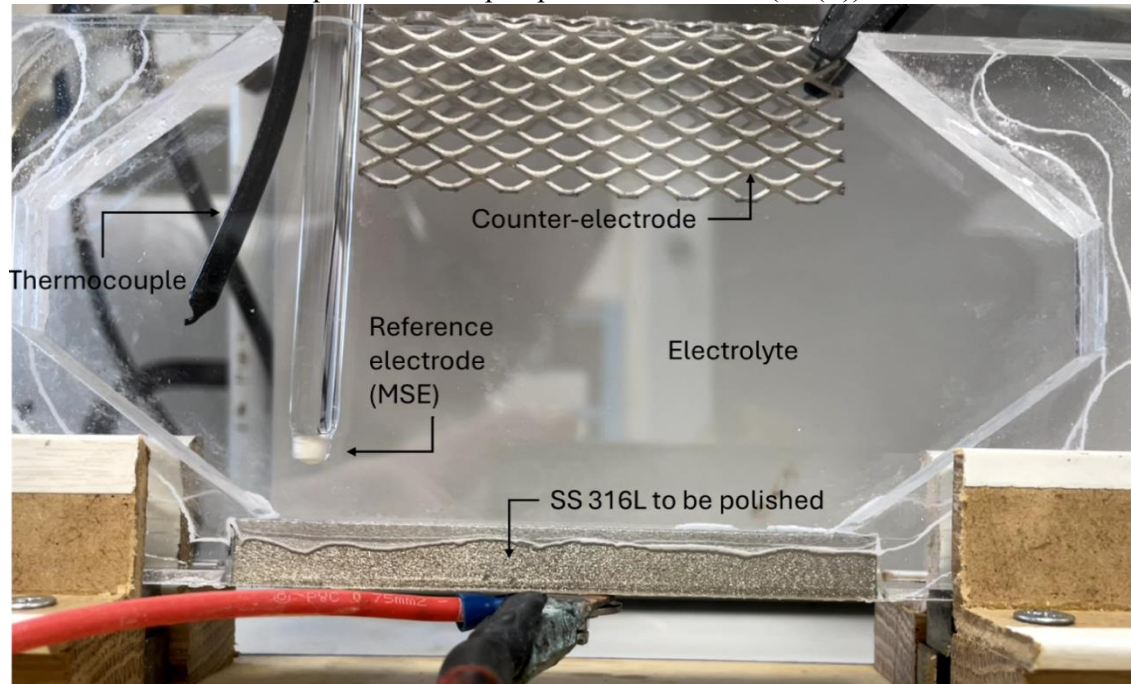

Figure 1: Photography of the specific cell developed for the experimentation

Linear sweep voltammetry was performed with a scan rate of 10 mV/s to assess the electrochemical behavior of SS 316L in the cell configuration. This allowed us to determine the potential ranges of interest for electropolishing: the polishing plateau and the beginning of solvent oxidation. Between each test, the electrolyte was mixed.

2.2 Optical characterization

Two techniques were used to characterize flows and movements in the liquid during electropolishing: Schlieren and PIV (Particle Image Velocimetry). Both these techniques are briefly described in the following sections, together with the setup used.

2.2.1 Schlieren imaging technique

The Schlieren imaging technique allows highlighting of small index variations in a transparent medium. More precisely, it is possible to render visible slight deviations of light rays due to small variations in the refractive index. It therefore offers better contrast than Shadowgraphy since it eliminates the parasitic "background", i.e. the undeflected rays. Its principle is shown in Figure 2 (left). Specifically, the rays depicted in gray on the figure, which do not encounter any change in refractive index, converge at the knife edge and are

subsequently blocked. Conversely, the rays shown in red, which cross a refractive index change, are deviated due to refraction. This deviation directs them toward the camera, thereby rendering the change in refractive index visible. During the electropolishing process, due to changes in the local composition of the mixture, a concentration gradient of the species present in solution is created, inducing a viscosity gradient and a refractive index gradient. In this way, the Schlieren technique enabled us to observe the phenomena governing electropolishing with a greater contrast. It was used both qualitatively for behavioral analysis and quantitatively/comparatively to analyze the growth of the viscous layer.

For spatial image calibration, a calibration test pattern was placed in front of and then behind the electrochemical cell (as the solution was too corrosive to allow a test pattern to be placed inside the device). The conversion factor is 26 pixels/mm. From the Schlieren imaging video, images were extracted to measure the thickness of the layer (Figure 2 right). The image processing carried out was the same for all the images obtained. The images were transcribed in 8 bits, and thresholded (with a threshold set at 14/255). Finally, 10 locations along the horizon axis were selected on the processed images. For all images, these locations were identical, and a boundary layer thickness measurement was performed at each point. For each image, a mean value of the boundary layer, taken over the 10 locations, was calculated. The error corresponding to determination of the layer thickness takes into account both the spatial calibration error and the standard deviation of the 10 measured values.
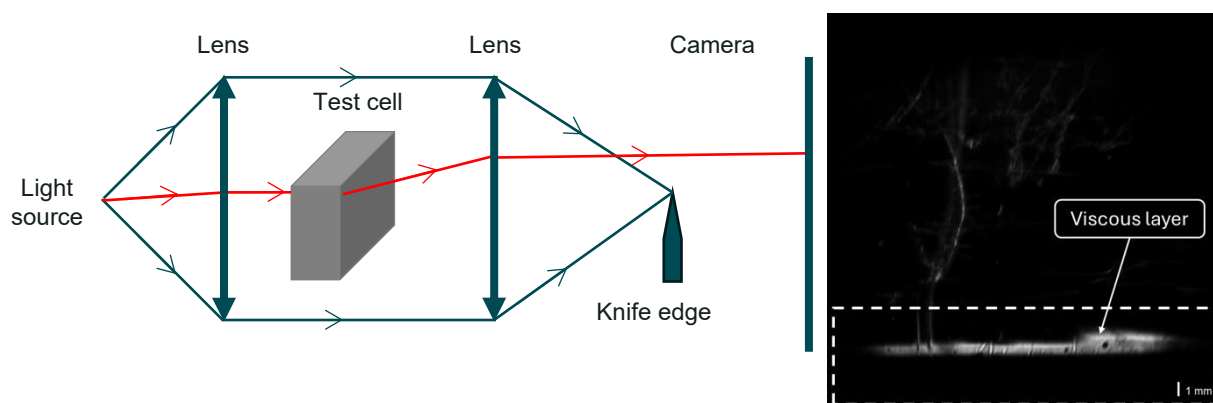

Figure 2: Schematic diagram of the Schlieren setup (left) and (right) example of snapshot taken during the recording under potentiostatic polarization at 1.85 V/SHE, showing viscous layer growth. The dotted area corresponds to the zone of interest detailed in Figure 10

2.2.2 Particle Image Velocimetry

PIV is a quantitative method, based on inter-correlation of image pairs, which provides velocity fields in the liquid. This technique enables qualitative and quantitative flow analysis using particles (tracers) dispersed in a fluid, in this case an electrolyte. More precisely, the fluid flow is seeded with tracers of sufficiently small size to follow the flow precisely. The area to be studied is illuminated with a laser sheet: the particles in the sheet will then scatter the light. Using a video acquisition system, successive images of the same flow plane are recorded. All the images are first pre-processed by shifting, averaging, and then removing average background, etc. Next, by dividing the images into windows of interest and correlating two spatially identical windows, it is possible to obtain the displacement of a given population of particles between the two shots. From this displacement, velocity is then deduced, and for each set of images, a velocity vector field is obtained. All pre-processing and processing were carried out using a program developed at the FEMTO-ST laboratory [22,23].

The PIV setup is shown in Figure 3. The laser source was a 632.8nm HeNe Laser (10mW HNL100L), and the acquisition camera was a PHANTOM-MIRO M120. Seeding the electrolyte with particles was not so simple. The highly acidic composition of the electrolyte was a specific challenge. To observe the viscous layer in the close vicinity of the wall, we would have needed to use fluorescent tracers, but those we thought were not chemically resistant to our electrolyte (amine not resistant to concentrated acids). Also, with sub-micrometric or micrometric but non-fluorescent particles, scattering was not sufficient to successfully process the images.

We were therefore unable to obtain usable PIV fields in the viscous layer. Thus, we focused our PIV study in a visualization window of about 1cm^2. The electrolyte was seeded in this case with silica particles of 9.98μm in diameter (SD=0.31μm). While the density of the electrolyte (approx. 1.56 g/cm^3) was lower than that of the silica particles (1.85 g/cm^3), the sedimentation times were much lower than the lowest macroscopic velocity observed. Furthermore, the Stokes number calculated in the worst-case scenario remained well below 1, so we can assume that the particles follow the flow faithfully.
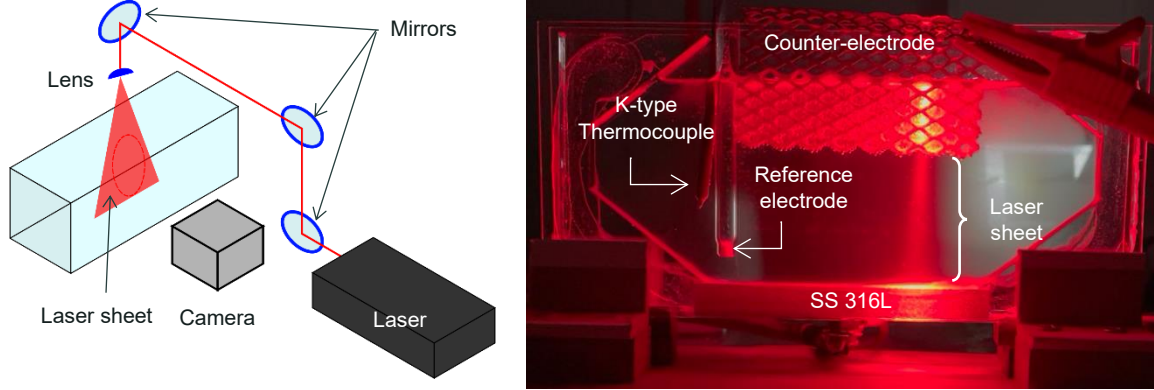
Figure 3: PIV diagram (left) and photo of the electropolishing assembly during the PIV process (right)

2.3 Chemical characterization: ICP

One of the causes of viscous layer establishment is the fast increase in dissolution product concentration (metallic cations) at the interface and their inability to diffuse rapidly to the bulk. The viscous layer is then much more concentrated in metallic cation than the bulk. Samples of the viscous layer were experimentally collected during electropolishing with a micropipette at surface vicinity until 1 mL was collected. The extraction was then analyzed by ICP-OES to determine the iron concentration. SS 316L is a single-phase alloy that dissolves homogeneously. Based on the alloy's iron, chromium, and nickel content, the iron concentration was extrapolated to the total dissolved cation concentration. This value will then be used as a threshold to determine the boundary between the viscous layer and the bulk in the simulation model.

3 Model formulation

The modeled geometry consists of a vertical plane of the specific cell described above. The upper boundary is cut, and the red line in Figure 4 corresponds to the counter-electrode while the blue line represents the workpiece. The electrolyte is defined as the gray area between the two. The reference electrode and the thermocouple are both disregarded. The change in geometry due to anode dissolution is not modeled since the dissolved thickness is assumed to be irrelevant in comparison to the inter-electrode distance (7 cm).
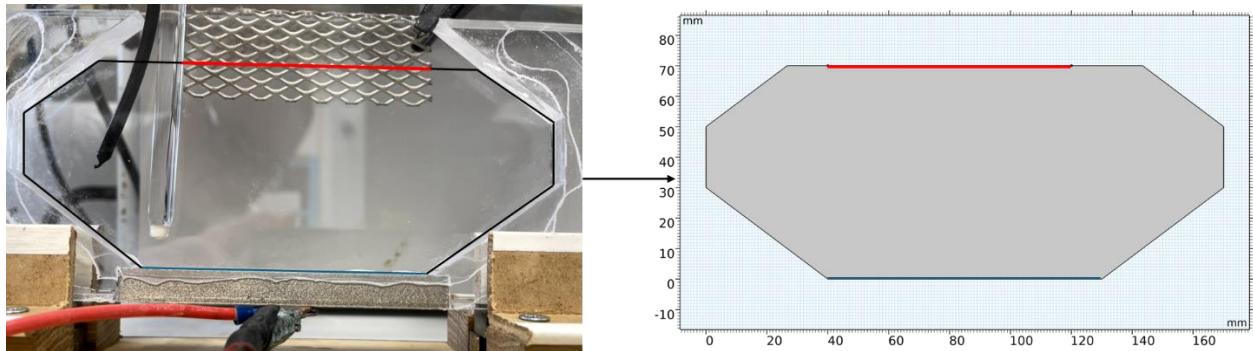

Figure 4: Photography of the specific cell and the transversal cut used as geometry for the simulation

The mesh is built in three steps. First, the edge representing the active surface is split into elements 25 µm apart. Then, the overall area is covered with free triangles. The mesh parameters are described in Table 1. The last step consists in refining the elements near the surface with boundary layers. 55 layers are built from the surface (Figure 5). The thickness of the first layer and the growth are 10 µm and 1.02, respectively. The mesh consists of 562072 elements.

Table 1: Mesh parameters

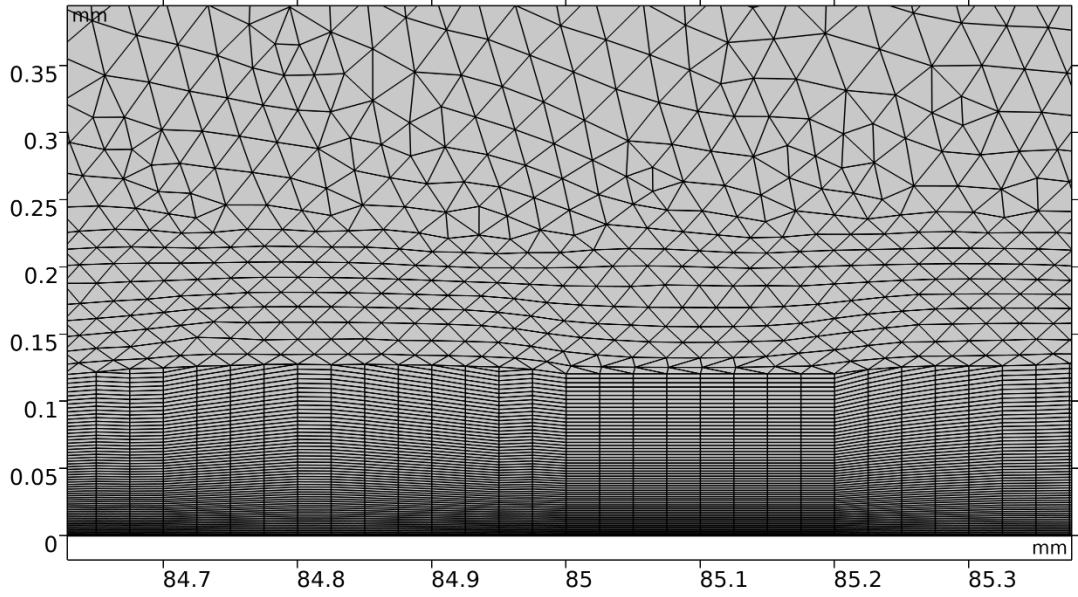| Predefined setup	CFD based mesh – extremely fine configuration
Max size of element	469 µm
Min size of element	1.4 µm
Growth rate	1.05
Curvature factor	1.2
Thin region resolution	1

Figure 5: Zoom on the mesh near the active surface (line at 0 mm) exhibiting boundary layers (rectangles) and the rest of the mesh (free triangles)

3.1 Tertiary current distribution

An important step in model definition is to determine the current distribution mode (primary, secondary or tertiary) to be solved. The model most often used is secondary current distribution (Equation 2), as it is the best compromise between primary distribution (Equation 1), which is not sufficiently predictive as it does not integrate reaction kinetics, and tertiary distribution (Equation 3), which is too complex to be solved with reasonable calculation times. In this work, since the volume of electrolyte considered is restricted and the aim is to highlight the viscous layer, characterized by metal cation concentration, it is possible to implement a tertiary current distribution.

Primary distribution (Ohm's law)	$i = -\sigma . \nabla\phi$	*Equation 1*
Secondary distribution (Butler-Volmer)	$i = i_0(e^{\frac{\alpha_a F\eta}{RT}} - e^{-\frac{\alpha_c F\eta}{RT}})$	*Equation 2*
Tertiary distribution (Nernst-Planck)	$i = -F \sum D_i z_i \nabla c_i - \frac{F^2}{RT}\nabla\phi \sum z_i^2 D_i c_i + u \sum z_i c_i$	*Equation 3*

where:

i	: current density (A.dm^{-2})	σ	: conductivity (S.m^{-1})
ϕ	: potential (V)	i_0	: exchange current density (A.dm^{-2})
η	: activation overpotential (V)	α_c	: so-called cathodic charge transfer coefficient (dimensionless)
α_a	: so-called anodic charge transfer coefficient (dimensionless)	T	: temperature (K)
F	: Faraday constant (~ 96485 C.mol^{-1})	R	: universal gas constant ($\sim 8,314$ J.K^{-1}.mol^{-1})
D_i	: diffusion coefficient (m^2.s^{-1})	z_i	: number of electrons involved in the electrode reaction (dimensionless)
c_i	: concentration (mol.m^{-3})	u	: velocity field (m.s^{-1})

No forced convection will be applied to the system, so that the convective part (the last term) of the Nernst-Planck equation can be removed. The two transport modes are diffusion and electromigration. There is no work available in the literature on characterizing the diffusion coefficients of the various species involved (oxidizing species, complexing species, dissolution products, etc.). Nevertheless, several works have shown that the electropolishing mechanism of 316L stainless steel is governed by the theory of an acceptor species [30]. It would therefore be the diffusion of this species, from the core of the solution toward the interface, which limits dissolution of the steel (see Figure 6).
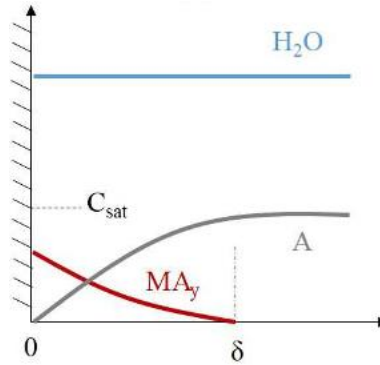

Figure 6: Schematic illustration representing the concentration profiles of anion and complex formed within the framework of the theory based on acceptor species limiting electropolishing

In this case, each anion (A) transported to the interface is instantly consumed by a dissolved metal cation (M) to form a complex ([MA$_y$]). It is assumed that complexing of 316L dissolution products by electrolyte anions forms the basis of the viscous layer. In the present electrolyte (a phospho-sulfuric acid mixture), it has already been pointed out that the main role of sulfuric acid in this electrolyte is to attack the oxide layer formed on the steel surface during anodic polarization [31]. Phosphoric acid, on the other hand, serves as a complexing agent for metallic ions. However, it is not impossible for both acids to play both roles. Based on these assumptions, formation of the viscous layer can be explained by the following mechanism:

- Steel $\square$ Steel$^+$ + 1 e$^-$ (purely electrochemical reaction)
- Steel$^+$ + A$^-$ $\square$ [SteelA] (complexing of dissolved metal cation by the acceptor species)
- Solvation and diffusion of [SteelA] from the interface to the bulk

The tertiary current distribution model will therefore be parameterized as follows. The dissolution kinetics is based on experimental oxidation rate characterization. The use of an "equivalent gram" for each electron exchanged allows the overall anode reaction to be considered: Steel $\square$ Steel$^+$ + 1 e$^-$, and an inflow (from the surface into the electrolyte) corresponding to formation of the Steel$^+$ cation to be defined. The second step corresponds to Steel$^+$ cation complexing by the acceptor anion A$^-$, according to: Steel$^+$ + A$^-$ $\square$ [SteelA]. This mechanistic part will not be simulated in the model as the reaction constants needed to describe this reaction accurately are not available. Thus, the complexing reaction will be treated as instantaneous. This will be reflected in the model by the assimilation of the Steel$^+$ concentration to the [SteelA] concentration. Finally, this

[SteelA] complex will be solvated and then diffused from the interface to the bulk. The various forms of phosphate present in the solution are meant to be the acceptor species. Given the concentrations of phosphoric and sulfuric acids in the electrolyte, the two predominant forms would be H_3PO_4 and/or $H_2PO_4^-$. As no diffusion coefficient values of such metal cations in this type of electrolyte are available in the literature, the diffusion coefficient of the complex will be assumed to be equal to the diffusion coefficient of phosphates in water. Chung et al. [32] gave a value of $2.61.10^{-12}$ m²/s in water for this coefficient, but another work by Edwards and Huffman [33] provided a curve plotting its evolution vs. concentration of phosphoric acid in water (Figure 7).
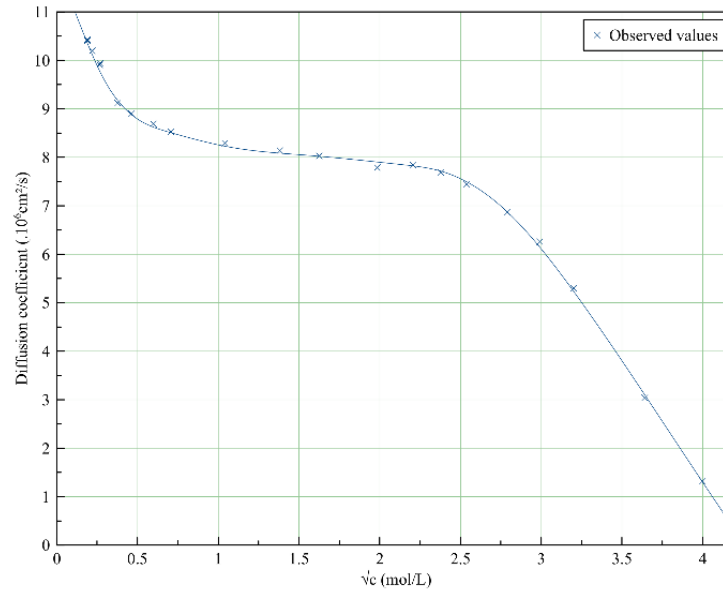

Figure 7: Evolution of diffusion coefficient as a function of the square root of concentration of phosphoric acid in water at 25°C [33].

Moreover, a predefined temporary solver proposed by Comsol Multiphysics® is used, and simulations correspond to electropolishing experiments over 300s, with extraction of results every 30s.

4 Results and discussion

4.1 Potentiodynamic polarization

4.1.1 Electrochemical characterization

An intensity-potential curve is drawn to establish the electrolyte's ability to electropolish the substrate in this specific configuration. This curve is obtained by recording the current during a linear potential sweep.
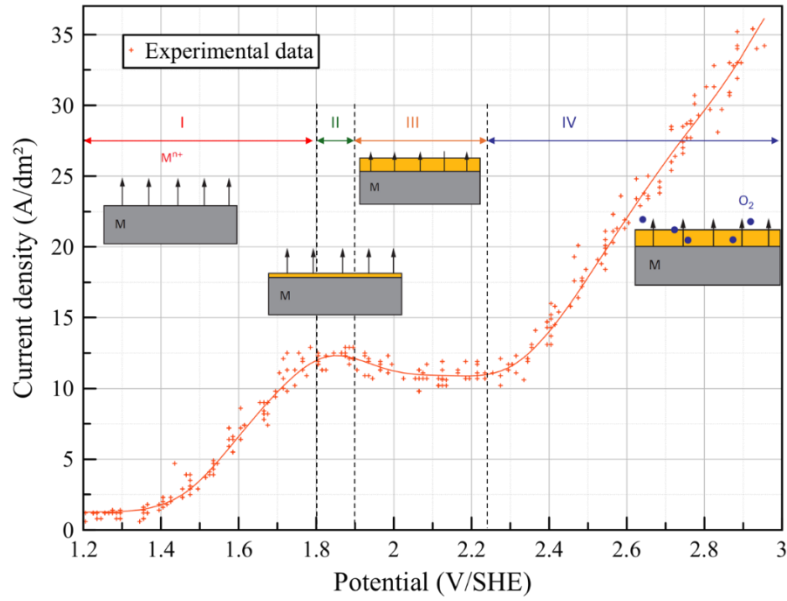
Figure 8: Linear sweep voltammetry exhibiting the polishing plateau (ability of the electrolyte to electropolish the substrate) adapted from [5]

The characteristic zones of a typical intensity-potential curve of anodic polarization of a metal in an electrolyte to electropolish are observed here [5]. Until up to around 1.7 V/SHE, active dissolution of the metal is described by a rise in current when the potential is increased (zone I). Around 1.8 V/SHE, current stabilization signals the establishment of the viscous layer (zone II). From 1.8 to 2.2 V/SHE, current remains almost constant when the potential is increased: the viscous layer is growing. This corresponds to the so-called electropolishing plateau (zone III). Above 2.3 V/SHE, a sharp increase in current is noticed associated with solvent oxidation (zone IV).

4.1.2 Simultaneous optical characterization

Standard quality videos were captured while the polarization curve was being drawn. Snapshots are listed in Figure 9. Formation of the viscous layer is evidenced by the orange-yellow layer appearing on the anode surface at potentials between 1.6 and 1.85 V/SHE. The color of the layer then intensifies, a sign that it is growing. From roughly 2.0 V/SHE, bubbles can be detected. While this is earlier than solvent oxidation, with the positioning of the reference electrode this can be attributed to edge effects. The local potential there is higher, which explains the early outgassing. Gas evolution at the edge of the part, visible under the reference electrode, occurs at around 2.35 V/SHE. This corresponds to the beginning of solvent oxidation on the intensity-potential curve. Intense gas evolution then increasingly unsettles the viscous layer. As the potential increases, so does the amount of gas produced.
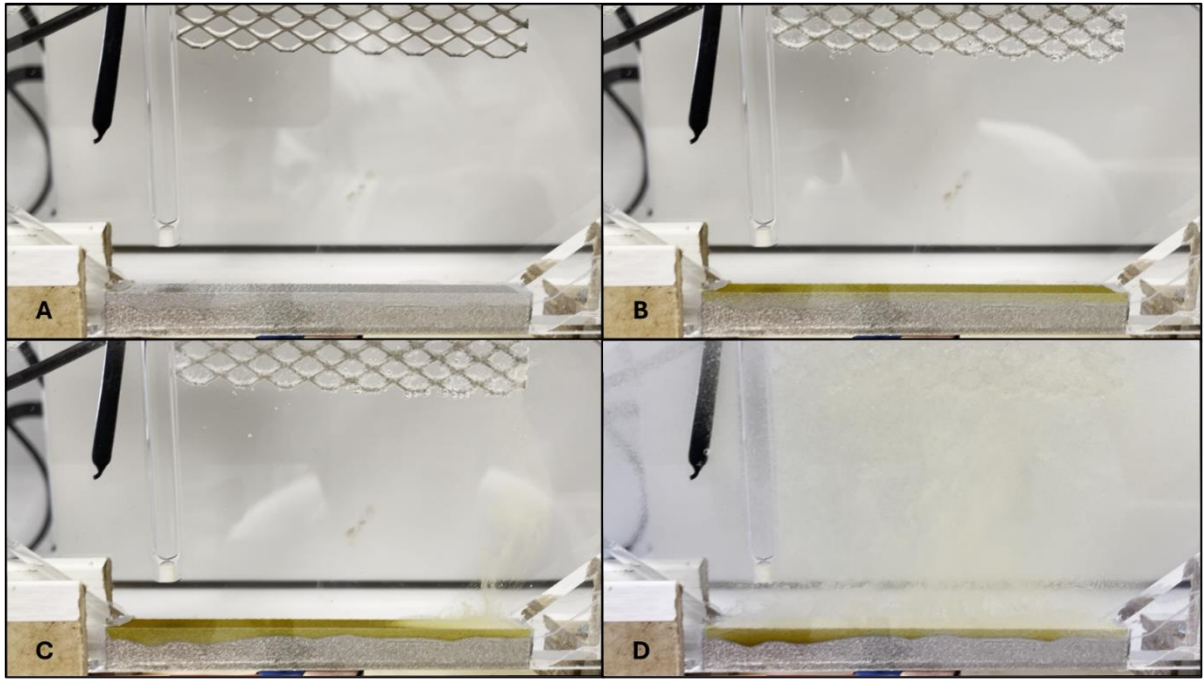
Figure 9: Snapshots taken during the polarization curve at: A 1.4 V/SHE (zone I), B 1.85 V/SHE (zone II), C 2.15 V/SHE (zone III), and D 2.75 V/SHE (zone IV)

4.2 Electropolishing under potentiostatic control on the polishing plateau

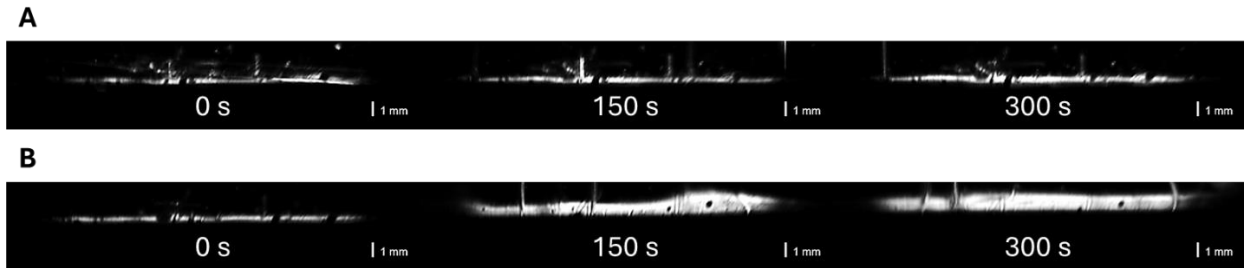### 4.2.1 Optical characterization without any polarization

Figure 10: Snapshots taken during the recording: A without any polarization showing native layer growth and bubble formation and B under potentiostatic polarization at 1.85 V/SHE showing viscous layer growth

Without polarization, no viscous layer is visible on the standard quality video. However, during optical characterization it was found that even without the application of potential, a native layer grew on the surface. This layer could be attributed to spontaneous corrosion of stainless steel in this mixture of mineral acids, as a few bubbles are observed simultaneously. Growth rate is determined from image analysis during the 420s of video (Figure 10 A). The native layer grows at a rate of around 0.85 μm/s.

4.2.2 Schlieren imaging of the viscous layer

Since it was established that a viscous layer forms over a certain potential range, tests were carried out under potentiostatic control. A potential of 1.85 V/SHE was applied for 5 min to characterize growth of the viscous layer. Likewise, snapshots were extracted during the recording in order to estimate its thickness (Figure 10 B). The measured thicknesses were then analyzed and plotted against time (Figure 11). Growth of the viscous layer exhibited a two-step evolution against time. During the first 120 s of polarization, the viscous layer grew rapidly,

then a slowdown was observed. This can be partially explained by the emergence of lateral convective movements in the cell.
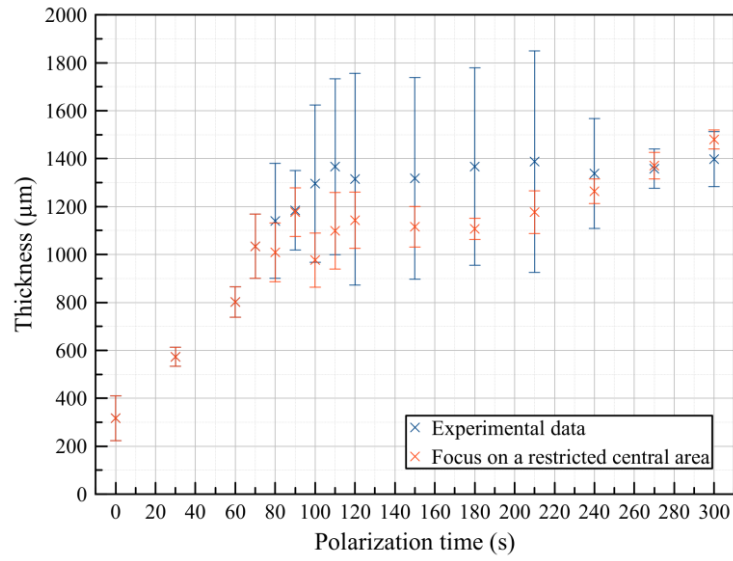

Figure 11: Viscous layer thickness evolution versus time

This first evolution of thickness over time (from 30 s to 110 s) was fitted using log-log representation (Figure 12 left). The linear regression on the log-log graph displays a slope of 0.52. This suggests that this behavior could be adjusted by the Cottrell law (Equ.4), in agreement with the electropolishing mechanism reported to be under diffusional control. Once fitted upon experimental data (red curve on the right in Figure 12), it leads to an equivalent diffusion coefficient: $D \approx 3.01.10^{-9}$ m²/s. This value is consistent with diffusion coefficients of common ions, such as phosphate, in water [34]. However, the Cottrell law is not able to predict the limiting thickness achieved by the viscous layer under stationary conditions (over 100 s).
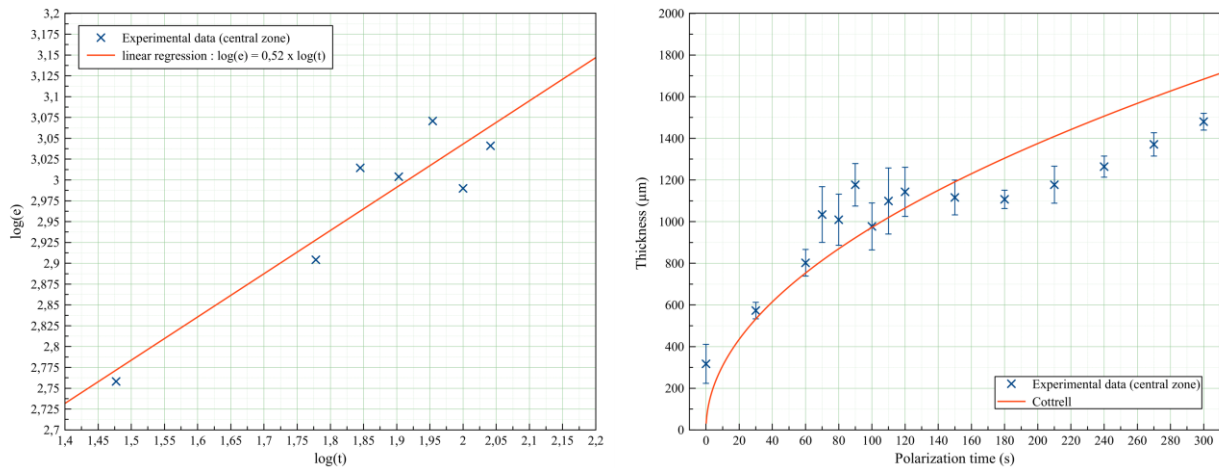

Figure 12: Viscous layer thickness versus time plot as log-log representation (left) and Cottrel law fit (right)

Cottrell law $$e = \sqrt{\pi D t}$$ *Equation 4*

where:

e : *viscous layer thickness (µm)* D : *diffusion coefficient (m^2/s)*

t : *time (s)*

Viscous layer growth rate can be determined from experimental data measured on the central zone. During the first 120s, the layer grows at a rate of approximately 6.04 µm/s, after which it drops to roughly half of that rate: 3.12 µm/s. Both viscous layer growth rates are much bigger than the rate at which the native layer grows without polarization.

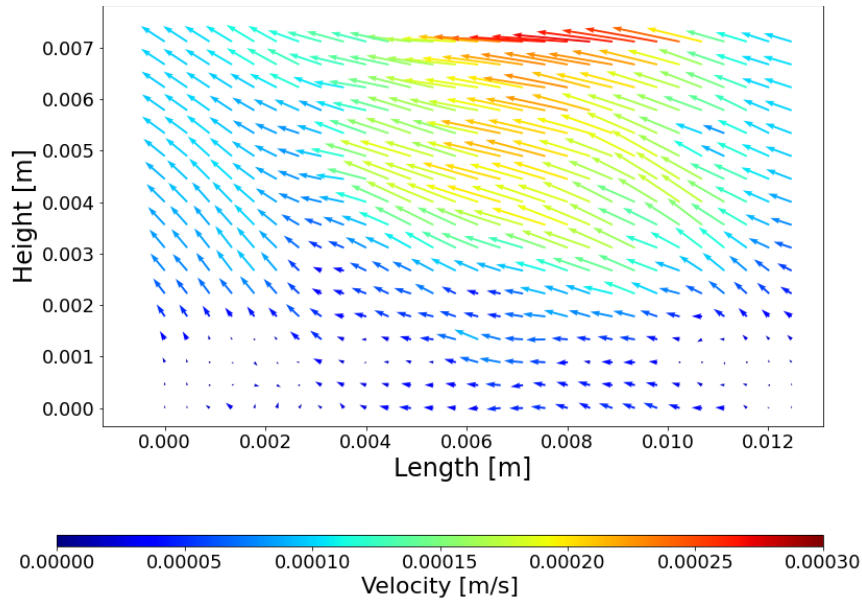### 4.2.3 Optical characterization (PIV)

Figure 13: Velocity field obtained by PIV during electropolishing at 1.85 V/SHE after 300s of polarization

Figure 13 shows the velocity vector field during polishing at 1.85 V/SHE after 5 minutes of polarization. It should be noted that the origin on the height axis does not correspond exactly to the surface, as the laser sheet causes a significant reflection of light at the surface, preventing analysis in this zone. There is therefore an offset of several tens of microns. Different zones in the velocity vector field can be noticed. At heights between zero and about one millimeter, it is interesting to observe that the norms of the velocity vectors are particularly low: < 50 µm/s. Moreover, orientation of these vectors seems to be predominantly parallel to the surface with no normal component in this observation zone situated slightly above the surface. PIV can therefore be used to extract information and highlight the presence of a zone in which the flow is very different from the rest of the electrolyte. However, with the characterizations carried out for the moment, it is not conceivable to attempt a more precise determination of the thickness of this layer, which seems to correspond to the viscous layer.

In the upper part, i.e. from a height of around three millimeters, the liquid moves with a much more pronounced biaxial component. The coupled vertical and horizontal movements are attributed to the combined effect of natural convection and liquid recirculation in the electrolyte. In fact, the change in composition of the mixture, combined with a slight heating of the wall (Joule Effect in particular), will induce upward convective movements in the cell, which is certainly what affects the evolution of the viscous layer after 110 s (Figure 11). On the other hand, during electropolishing, gas is released from the wall, particularly at the ends of the cell, due to electrochemical edge effects. As the bubbles grow and detach, they carry liquid in their wake. These upward movements will induce recirculation rolls. The norm of the velocity vectors in this zone is systematically greater than 1 mm/s, which is much higher than in the zone assumed to be the viscous layer.

4.2.4 Modeling growth of the viscous layer under potentiostatic conditions

The simulation model was used to predict evolution of the viscous layer over time. The tertiary current distribution model is used to predict concentration of metal cation formed during polarization. The interface between the viscous layer and the bulk is set according to a threshold concentration value: measured experimentally by ICP analysis from viscous layer samples taken during experimental tests. Two diffusion coefficients from the literature (constant (dotted line) and concentration-dependent (solid line)) were used, and the results of the two calculations were compared (Figure 14), as well as a simulation using the diffusion coefficient obtained using Cottrel law fit on experimental data (dashed line).
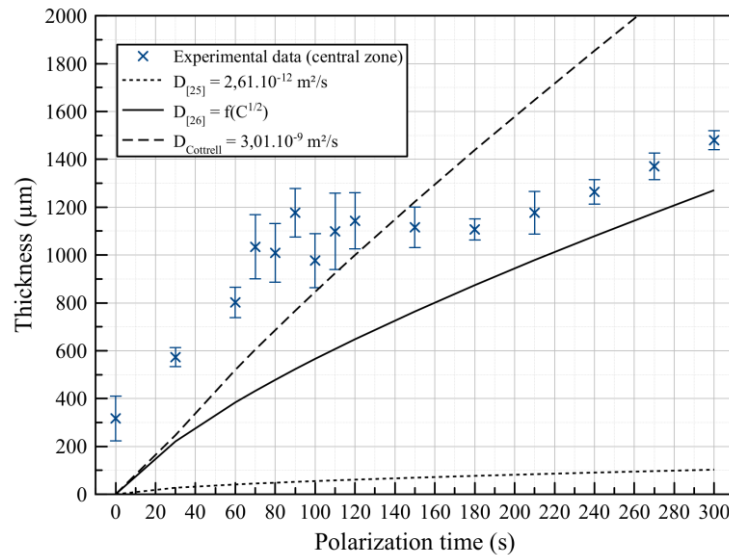

Figure 14: Prediction of viscous layer thickness against time for the two different diffusion coefficients used in the tertiary current distribution model

Using the diffusion coefficient, determined by the law described in Chung et al. [32], viscous layer thickness is far too low: 100 μm after 300s of polarization compared with 1400 μm experimentally. Thickness after the test would even be less than that observed without polarization. Moreover, the predicted maximum surface concentrations are already around 30 mol/L after 30s, which is impossible given that the concentration of 85 %$_w$ phosphoric acid (the most concentrated commercially available) is 14.6 mol/L (Figure 15 A). This model is therefore not satisfactory for reproducing the expected behavior.
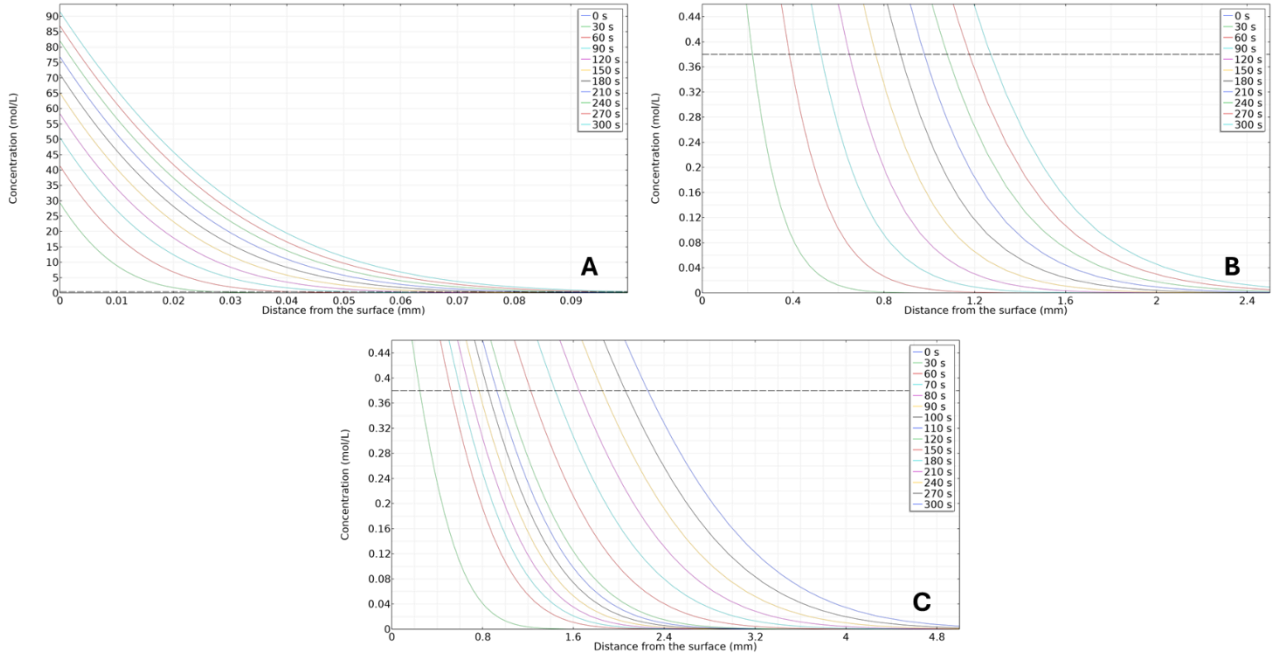
Figure 15: Concentration profile obtained with the tertiary current distribution model using diffusion coefficient A constant from [32], B varying with local concentration [33], and C determined by fitting a Cottrel law on experimental data.

Using the diffusion coefficient determined by fitting a Cottrell law on the experimental data (Figure 15 C) does not allow good reproduction of evolution of layer growth throughout polarization. Therefore, the equivalent diffusion coefficient extracted from this law cannot be used as input data for a tertiary current distribution-based model.

Finally, variation in diffusion coefficient with concentration, as proposed by Edwards and Huffman [33], allows better adjustment of the experimental results (Figure 14 and Figure 15 B), although there is a continuous underestimation of thickness. This can be attributed to the initial thickness of the layer observed at the beginning of polarization (Figure 11: t = 0s). An additional step was to add to this curve the initial thickness value at the beginning of the record (before polarization) equal to 317 μm (dashed line on Figure 16). In this way, the model is in good agreement with experimental characterizations.
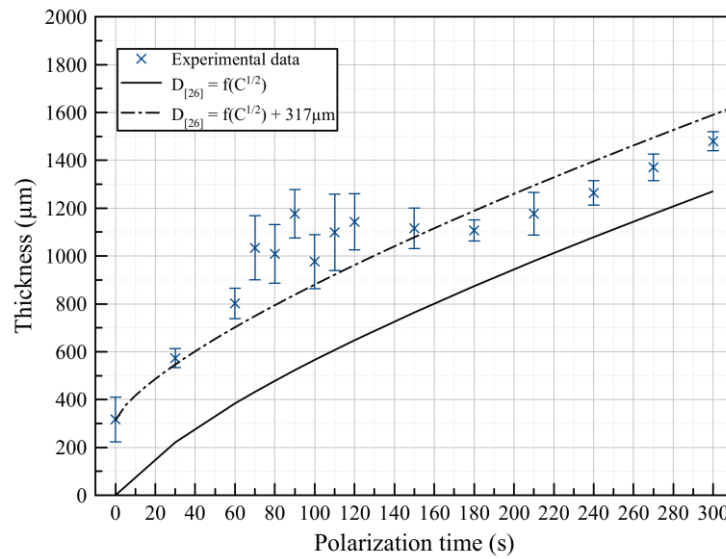

Figure 16: Prediction of viscous layer thickness against time using variation in diffusion coefficient with concentration and shift corresponding to the 317 μm of viscous layer observed at the beginning of recording

5 Conclusion

This work provides a complete study of the establishment of a viscous layer during electropolishing of 316 L stainless steel produced by metal additive manufacturing in a mixture of mineral acids. Optical characterization at different scales validates the potential ranges at which the viscous layer forms and grows, before being destabilized by gas evolution during solvent oxidation. Schlieren imaging helps estimate thickness of the viscous layer after 5 minutes' polarization at the beginning of the polishing plateau: approximately 1.4 mm, which is about one millimeter thicker than its natural thickness without polarization. PIV characterizations confirm a zone of roughly one millimeter thickness with no perpendicular flow to the surface, distinct from the bulk where natural convection was observed.

A simplified reaction mechanism is proposed, based on experimentally determined reaction kinetics reported for each electron exchanged. The cations are assumed to be instantaneously complexed. The assumption is made that diffusion of this complex is the same as that of the free complexing agents (phosphates), taken from the literature. From this, a tertiary current distribution model was developed and successfully reproduced growth of the viscous layer, based on these assumptions. Indeed, an experimental characterization of metallic cation concentration in the viscous layer served as a threshold to determine the limit of the viscous layer from the model's local concentration predictions. This agreement between the experimental results and the model predictions validates the theory that "acceptor" species diffusion is the main driving force behind polishing. Moreover, this work confirms the hypothesis that metal cations are complexed by phosphate and that diffusion of complexes is analogous to that of anions.

Perspectives of this work on characterization of the viscous layer, which governs the electrochemical polishing process, consist of two main areas. First, characterizations of layer growth could be substantiated at different potentials on the polishing plateau and compared with material removal and roughness reduction obtained under these conditions. Second, electrolytic polishing of additively manufactured parts is generally performed by means of agitation. The impact of agitation on viscous layer stability would need to be characterized to further enhance understanding of the different phenomena governing the polishing mechanisms.

6 Acknowledgements

7 References

[1]   F. Laverne, P. Dubois, Additive manufacturing General principles, Techniques de l'ingénieur (2016).

[2]   S. Pillot, Fusion laser sélective de lit de poudres métalliques, Techniques de l'ingénieur (2016).

[3]   E. Yasa, Selective laser melting, in: Addit Manuf, Elsevier, 2021: pp. 77–120. https://doi.org/10.1016/B978-0-12-818411-0.00017-3.

[4]   M.-L. Doche, J.-Y. Hihn, Procédé pour le parachèvement des pièces de fabrication additive métalliques, Techniques de l'ingénieur (2021).

[5]   M.-L. Doche, J.-Y. Hihn, A. Mandroyan, E. Drynski, C. Rotty, Y. Dugenet, J. Tardelli, L'électropolissage: un outil pour le post - traitement des pièces de fabrication additives, (2018) 28–32. http://www.irt-m2p.eu/UserFiles/File/presse/201812-traitements-et-materiaux-455-after-alm.pdf.

[6]   P.A. Jacquet, H. Figoux, Perfectionnement aux traitements électrolytiques des métaux., 707526, 1930.

[7]   P.A. Jacquet, Electrolytic Method for obtaining Bright Copper Surfaces, Nature 135 (1935) 1076. https://doi.org/10.1038/1351076c0.

[8]   W.C. Elmore, Electrolytic Polishing, J Appl Phys 10 (1939) 724–727. https://doi.org/10.1063/1.1707257.

[9] W.C. Elmore, Electrolytic Polishing. II, J Appl Phys 11 (1940) 797–799. https://doi.org/10.1063/1.1712738.

[10] D. Landolt, Fundamental aspects of electropolishing, Electrochim Acta 32 (1987) 1–11. https://doi.org/10.1016/0013-4686(87)87001-9.

[11] V.G. Levich, Physicochemical Hydrodynamics, Prentice-Hall, 1962.

[12] T.P. Hoar, J. a. S. Mowat, Mechanism of Electropolishing, Nature 165 (1950) 64–65. https://doi.org/10.1038/165064a0.

[13] J.P. Diard, P. Landaud, J.M. Le Canut, B. Le Gorrec, Interprétation cinétique du palier de polissage électrolytique des métaux, in: Montrouge, 1992.

[14] S. Magaino, M. Matlosz, D. Landolt, An Impedance Study of Stainless Steel Electropolishing, J Electrochem Soc 140 (1993) 1365–1373. https://doi.org/10.1149/1.2221562.

[15] M. Matlosz, S. Magaino, D. Landolt, Impedance Analysis of a Model Mechanism for Acceptor-Limited Electropolishing, J Electrochem Soc 141 (1994) 410–418. https://doi.org/10.1149/1.2054741.

[16] C. Rotty, M.-L. Doche, A. Mandroyan, J.-Y. Hihn, G. Montavon, V. Moutarlier, Comparison of electropolishing behaviours of TSC, ALM and cast 316L stainless steel in H_3PO_4/H_2SO_4, Surfaces and Interfaces 6 (2017) 170–176. https://doi.org/https://doi.org/10.1016/j.surfin.2017.01.008.

[17] M.-L. Doche, J.-Y. Hihn, E. Drynski, F. Roy, A. Boucher, J. Rolet, J. Tardelli, Electropolishing of 316L stainless steel parts elaborated by selective laser melting: from laboratory to pilot scale, Procedia CIRP 108 (2022) 722–727. .

[18] H. Warlimont, A. Koethe, Springer Handbook of Materials Data, 2nd ed., Springer International Publishing, 2018. https://doi.org/10.1007/978-3-319-69743-7.

[19] O. Dubrovski, S. Tietze, A. Zigelman, K.S. Drese, G. Lindner, O. Manor, The Enhancement of Ion Transport in an Electrochemical Cell Using High Frequency Vibration for the Electropolishing of Copper, J Electrochem Soc 165 (2018) E236. https://doi.org/10.1149/2.0811805JES.

[20] M.I. Nave, Y.C.K. Chen-Wiegart, J. Wang, K.G. Kornev, Precipitation and surface adsorption of metal complexes during electropolishing. Theory and characterization with X-ray nanotomography and surface tension isotherms, Physical Chemistry Chemical Physics 17 (2015) 23121–23131. https://doi.org/10.1039/C5CP03431K.

[21] E.J.F. Dickinson, H. Ekström, E. Fontes, COMSOL Multiphysics®: Finite element software for electrochemical analysis. A mini-review, Electrochem Commun 40 (2014) 71–74. https://doi.org/10.1016/j.elecom.2013.12.020.

[22] M. Hackert, G. Meichsner, A. Schubert, Simulation of the Shape of Micro Geometries Generated with Jet Electrochemical Machining, Comsol Conference Hannover (2008). https://www.comsol.com/paper/simulation-of-the-shape-of-micro-geometries-generated-with-jet-electrochemical-m-5106.

[23] R. Paul, M. Hackert-Oschätzchen, I. Danilov, M.Y. Zanjani, A. Schubert, 3D Multiphysics Simulation of Jet Electrochemical Machining of Intersecting Line Removals, Procedia CIRP 82 (2019) 196–201. https://doi.org/10.1016/j.procir.2019.04.154.

[24] F. Klocke, M. Zeis, S. Harst, A. Klink, D. Veselovac, M. Baumgärtner, Modeling and Simulation of the Electrochemical Machining (ECM) Material Removal Process for the Manufacture of Aero Engine Components, Procedia CIRP 8 (2013) 265–270. https://doi.org/10.1016/j.procir.2013.06.100.

[25] F. Klocke, L. Heidemanns, M. Zeis, A. Klink, A Novel Modeling Approach for the Simulation of Precise Electrochemical Machining (PECM) with Pulsed Current and Oscillating Cathode, Procedia CIRP 68 (2018) 499–504. https://doi.org/10.1016/j.procir.2017.12.081.

[26] M. Bruchon, B. Visentin, F. Eozénou, Electropolishing on single and multi-cell: COMSOL modelling, Beijing, China, 2007. http://cds.cern.ch/record/1091551?ln=fr.

[27] L.M.A. Ferreira, H. Rana, Electropolishing simulation on full scale radio frequency elliptical structures, Chicago, IL, USA, 2014. http://accelconf.web.cern.ch/AccelConf/LINAC2014/papers/thpp029.pdf.

[28] D. Bonnet, Vélocimétrie par images de particules (PIV) pour le diagnostic d'écoulements dans la boucle d'air automobile, FEMTO - ST, 2012. https://theses.hal.science/tel-00978193.

[29] D. Bonnet, M. Barthès, Y. Bailly, L. Girardot, D. Ramel, A. Grenier, D. Guyon, PIV in a running automotive engine: simultaneous velocimetry for intake manifold runners, Journal of Flow Visualization and Image Processing 19 (2012) 239–253. https://doi.org/10.1615/JFLOWVISIMAGEPROC.2013005843.

[30] C. Rotty, M.-L. Doche, A. Mandroyan, V. Vivier, J.-Y. Hihn, Mechanistic Study of Cast and 3D-Printed Stainless Steel Electropolishing in Acid Media and Deep Eutectic Solvents, J. of Electrochem Soc. S 169 (2022) 071504. https://doi.org/10.1149/1945-7111/AC7BB3.

[31] C. Rotty, Etude de l'électropolissage d'alliages horlogers issus de fabrication additive en milieu aqueux et solvant non-conventionnel, Bourgogne Franche-Comté, 2018. http://www.theses.fr/2018UBFCD017.

[32] S.H. Chung, S. Bajue, S.G. Greenbaum, Mass transport of phosphoric acid in water: A 1H and 31P pulsed gradient spin-echo nuclear magnetic resonance study, J Chem Phys 112 (2000) 8515–8521. https://doi.org/10.1063/1.481454.

[33] O.W. Edwards, E.O. Huffman, Diffusion of Aqueous Solutions of Phosphoric Acid at 25°, J Phys Chem 63 (1959) 1830–1833. https://doi.org/10.1021/j150581a011.

[34] L. Yuan-Hui, S. Gregory, Diffusion of ions in sea water and in deep-sea sediments, Geochim Cosmochim Acta 38 (1974) 703–714. https://doi.org/10.1016/0016-7037(74)90145-8.